Simple Dynamical Models of Neptune's Great Dark Spot

L. M. POLVANI,* J. WISDOM, E. DEJONG, A. P. INGERSOLL

The large amplitude oscillations of the shape of Neptune's Great Dark Spot are well reproduced by simple dynamical models of an isolated vortex embedded in a background shear flow. From the time series of the aspect ratio and inclination of the vortex values are estimated for the background shear and the mean vorticity of the Great Dark Spot, and a lower bound is placed on the value of the Rossby deformation radius. These models imply the existence of a planetary-scale zone of deterministic chaotic advection in the atmosphere of Neptune.

THE RECENT ENCOUNTER OF THE VOYAGER 2 SPACECRAFT with Neptune has revealed the presence of a large coherent structure in its atmosphere, dubbed the Great Dark Spot (*1*), which undergoes dramatic variations in its shape. We propose that the observed oscillations of the Great Dark Spot are the natural oscillations of a vortex in a background shear flow.

In view of the paucity of atmospheric features on Neptune the vorticity cannot be measured directly. By fitting the observed oscillations in shape to those of sheared elliptical vortices we obtain estimates of the background shear and the anomalous vorticity of the Great Dark Spot without using any knowledge of the velocity fields on Neptune. The vorticity is found to be larger than that of the ambient flow, as is the case for the Great Red Spot on Jupiter. Both vortices are anticyclonic.

We find that the latitudinal variation of the Coriolis parameter (the β effect) has little influence on the dynamics of the system. Our dynamical models suggest that the Rossby radius of deformation is larger than about two thirds of the diameter of the Great Dark Spot. Last, our models imply the existence of a planetary-scale zone of deterministic chaotic fluid motion in the atmosphere of Neptune.

Voyager image analysis. We analyzed 28 projected Voyager images, which were taken from the same images as figure 4A of Smith *et al.* (*1*). The projection used was linear in latitude and longitude, and centered at −19.6° latitude. These data span 31 Great Dark Spot rotation periods. The Great Dark Spot rotation period, namely the rotation period of the planet as defined by the Great Dark Spot, is approximately 18.3 hours. For comparison, the radio rotation period of Neptune is 16.11 hours.

We fit ellipses to the boundary of the Great Dark Spot with the aid of the SAOimage software, which allows an ellipse to be superimposed on the image and, with a pointer, to adjust the center, minor axis, major axis, and orientation of that ellipse. In most images we find that the shape of the Great Dark Spot is well represented by an ellipse (see, for instance, Fig. 1). In a few cases a tail is also present, but an elliptical core is still easily identified (as illustrated in Fig. 2); in these cases the elliptical core is taken to represent the vortex. Only in two images, during the ejection of the large tail, is the representation of the Great Dark Spot as an ellipse ambiguous. Table 1 gives the parameters of the fit ellipses. We define $\lambda (0 < \lambda < 1)$ to be the ratio of the minor to major axis, the inverse of the aspect ratio, and specify the orientation of the ellipse by the angle φ between the major axis and the zonal direction, measured counterclockwise.

Before settling on the manual elliptical fits, we tried a variety of different techniques to objectively extract the boundary of the Great Dark Spot from the images: clipping, gradient, laplacian, smoothing, all of these in various combinations. The boundaries determined by these methods were judged to be unsatisfactory representations of the Great Dark Spot as one sees it in the images. The main problem is caused by the presence of bright clouds which overlie the Great Dark Spot. These distort the boundaries determined by the simple objective methods. We did not try to develop a more sophisticated fitting algorithm which could automatically account for the presence of the clouds.

Because we had no objective method for fitting the boundary of the Great Dark Spot, we estimated the errors in our fits by repeating each fit independently several times (see Table 1). These error estimates rigorously only represent our ability to reproduce our own fits. The true errors are likely to be larger. For example, we did not correct for the fact that the projection of the images distorts the shape of the Great Dark Spot. Some uncertainty is also introduced by the presence of the bright clouds near the boundary of the Great Dark Spot (as can be seen from Fig. 2).

We note that the area of the Great Dark Spot as determined by our fit ellipses is nearly constant (Fig. 3), even though our fitting procedure was not geared toward an accurate determination of the area. This would have required more careful photometry. Rather, our fitting procedure was geared solely to determining the aspect ratio and orientation of the Great Dark Spot. The diameter of a circle with the same area as the Great Dark Spot, as determined by our fit ellipses, is $D = 9842 \pm 57$ km, excluding the first image and the last two images. The fit to the first image appears anomalous, both in the area of the vortex and in the orientation angle. The last two points show a marked decrease in the area which is associated with the ejection of a large tail. Despite these misgivings, all of the

L. M. Polvani is in the Department of Mathematics and J. Wisdom is in the Department of Earth, Atmospheric, and Planetary Sciences, Massachusetts Institute of Technology, Cambridge, MA 02139. E. DeJong and A. P. Ingersoll are in the Division of Geological and Planetary Sciences, California Institute of Technology, Pasadena, CA 91125.

*Present address: Department of Applied Physics, Columbia University, New York, NY 10027.

data points were used in the fits to the dynamical models presented in this paper.

Dynamical models. We compare the Voyager data to a hierarchy of simple models of the dynamics of the Great Dark Spot. In all of these the Great Dark Spot is taken to be a simple vortex in a background shear flow. The models are quasigeostrophic (*2*) and assume piecewise constant geostrophic potential vorticity inside and outside the vortex. Uniform potential vorticity is commonly observed in numerical simulations (*3*) and laboratory experiments (*4*).

In all of the models the dynamics is given by the material conservation of geostrophic potential vorticity Π (*5*):

$$\frac{D\Pi}{Dt} = 0 \tag{1}$$

with the material derivative

$$\frac{D}{Dt} = \frac{\partial}{\partial t} + J(\psi, \cdot) \tag{2}$$

where J is the Jacobian operator and $\psi = \psi_V + \psi_B$ is the total streamfunction, with ψ_V the component due to the vortex and ψ_B the component due to the background shear. The respective potential vorticities are Π_V and Π_B, and the relative vorticities are $q_V = \nabla^2\psi_V$ and $q_B = \nabla^2\psi_B$. We adopt local Cartesian coordinates (x, y), comoving with the zonal mean-motion of the Great Dark Spot, with positive x eastward and positive y northward. In terms of the streamfunction the velocity (u, v) is

$$u = -\frac{\partial\psi}{\partial y} \qquad v = \frac{\partial\psi}{\partial x} \tag{3}$$

Model 1—barotropic f-plane. The simplest model describes the dynamics of a single layer of rotating constant density fluid in which motions are two dimensional and quasi-geostrophic (*6*). This is known as the barotropic *f*-plane model. Ignoring the constant planetary vorticity, the potential vorticity is given by $\Pi = \nabla^2\psi$, which is simply the relative vorticity.

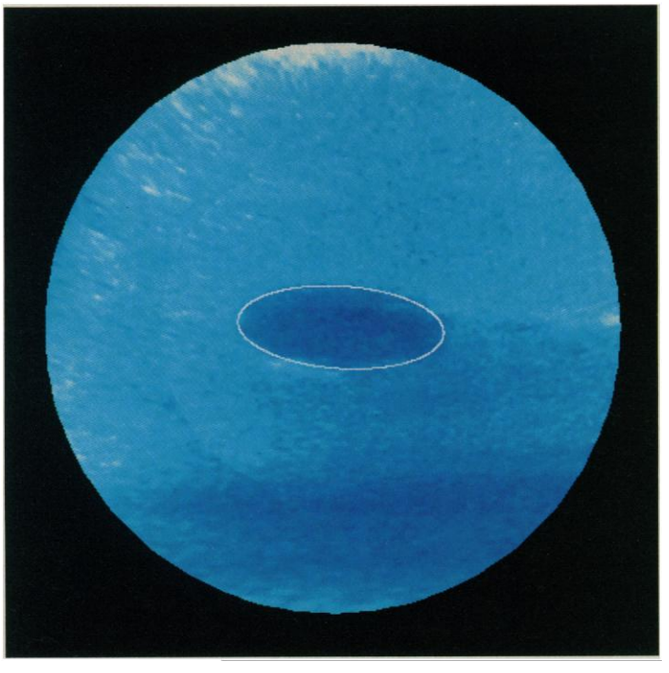

Fig. 1. A representative image showing the Great Dark Spot with our fit ellipse superimposed. The Great Dark Spot is usually well represented as an ellipse. This image corresponds to the sixth in the series presented in figure 4A of Smith *et al.* (*1*).

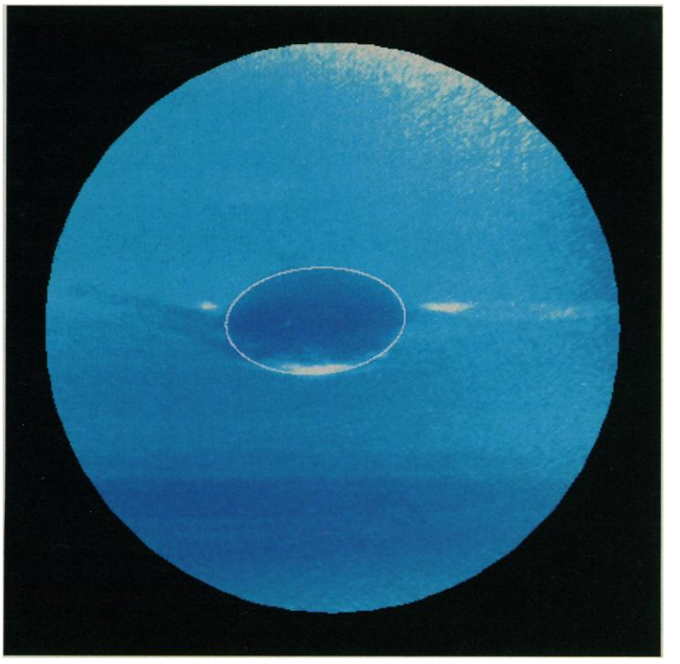

Fig. 2. An example of an image of the Great Dark Spot with an elliptical core and a tail. The ellipse was fit to the core. This image is the second one from the top in the rightmost column in figure 4A of Smith *et al.* (*1*).

In this model, the streamfunction ψ_V and ψ_B, associated with the vortex and the background, respectively, satisfies

$$\nabla^2\psi_V = \Pi_V \qquad \nabla^2\psi_B = \Pi_B \tag{4}$$

Thus Π_V and Π_B are simply the relative vorticities q_V and q_B. We take the background shear flow to be constant in time and uniform in space, with an associated streamfunction given by:

$$\psi_B = -\frac{1}{2} sy^2 \tag{5}$$

where s is the background shear and is also equal to the negative of the background vorticity q_B. The background velocity u_B is a simple linear shear

$$u_B = sy \tag{6}$$

We recall that, in this simplest case, an elliptical vortex patch is an exact nonlinear time-dependent solution of Eq. 1, widely known as the Kida vortex (*7*). The state of the system is entirely specified by λ, the inverse of the aspect ratio, and φ, the orientation of the vortex. These evolve according to:

$$\frac{d\lambda}{dt} = -s\,\lambda\sin 2\varphi \qquad \frac{d\varphi}{dt} = \Omega_K + \frac{s}{2}[-1 + \Lambda\cos 2\varphi] \tag{7}$$

where $\Omega_K = q_V\lambda/(1 + \lambda)^2$ is the angular velocity of the elliptical vortex patch in the absence of shear (a Kirchhoff vortex), and $\Lambda \equiv (1 + \lambda^2)/(1 - \lambda^2)$.

The vortex orientation angle φ can rotate or oscillate depending on the value of s/q_V, and the initial values of φ and λ. We have shown (*8*) that large zones of deterministic chaotic Lagrangian motion can exist around such vortices. These chaotic zones can produce rapid mixing in the surrounding fluid.

Model 2—barotropic β-plane. The next model also takes into account the latitudinal variation of the Coriolis parameter $f = 2\Omega\sin\vartheta$, where $2\pi/\Omega$ is the Great Dark Spot rotation period and ϑ is the latitude, which was approximately $-19.6°$ during the

Neptune encounter. The potential vorticity in this model is given by $\Pi = \nabla^2\psi + \beta y$, where $\beta = 2\Omega \cos \vartheta / R_{\text{Neptune}}$ is the derivative of f with respect to northward distance. This system is known as the quasi-geostrophic β-plane model.

Under the assumption of piecewise constant potential vorticity Π, the components ψ_V and ψ_B respectively satisfy

$$\nabla^2\psi_V = \Pi_V \qquad \nabla^2\psi_B + \beta y = \Pi_B = -s \tag{8}$$

From the second of these equations we obtain the expression for the streamfunction associated with the background shear:

$$\psi_B = -\frac{1}{2} s y^2 - \frac{1}{6} \beta y^3 \tag{9}$$

whereas ψ_V has to be determined numerically. The background velocity u_B associated with ψ_B is:

$$u_B = sy + \frac{1}{2} \beta y^2 \tag{10}$$

The uniform value of the potential vorticity inside the vortex is $\Pi = q_V + q_B + \beta y$.

Model 3—equivalent barotropic β-plane. The third model additionally allows for the presence of an infinitely deep lower layer rotating as a solid body at the 18.3-hour period of the Great Dark Spot. The effect of this lower layer is taken into account by defining the potential vorticity $\Pi = \nabla^2\psi + \beta y - \gamma^2\psi$, where γ is the inverse of the Rossby radius of deformation. This model is variously known as the equivalent barotropic or the reduced gravity model.

The components ψ_V and ψ_B respectively satisfy

$$\nabla^2\psi_V - \gamma^2\psi_V = \Pi \qquad \nabla^2\psi_B - \gamma^2\psi_B + \beta y = 0 \tag{11}$$

Note that in this model the potential vorticity associated with the background flow is identically zero, thus $\Pi_V = \Pi$.

For the background streamfunction, we choose the solution of the equation which reduces to the background streamfunction (*9*) of model 2 in the limit $\gamma \to 0$. This gives

$$\psi_B = \frac{\beta}{\gamma^2}\left[y - \frac{\sinh(\gamma y)}{\gamma}\right] - \frac{s}{\gamma^2}\cosh(\gamma y) \tag{12}$$

with the associated velocity field

$$\mu_B = -\frac{\beta}{\gamma^2}[1 - \cosh(\gamma y)] + s\left[\frac{\sinh(\gamma y)}{\gamma}\right] \tag{13}$$

Again, ψ_V must be obtained numerically.

Parameters. The unknown parameters of the models are the background shear s, the anomalous potential vorticity Π_V, and for model 3, γ the inverse of the Rossby radius of deformation. We note that β is given and at −19.6° latitude has the value 7.26×10^{-10} $\text{km}^{-1}\,\text{s}^{-1}$.

Numerical methods. In our models the gradient of potential vorticity is nonzero only on the boundary of the vortex, and the dynamics is uniquely determined by the position of that boundary. In model 1 the shape variations are governed by Eq. 7; in the other two models the evolution of the boundary must be computed directly from Eq. 1.

With the exception of model 1, vortices which are initially elliptical do not remain elliptical. We extract an equivalent aspect ratio and orientation of the vortex by computing the spatial moments up to second order of the area enclosed by the vortex boundary and then taking the aspect ratio and orientation to be those of an equivalent ellipse with the same moments.

The evolution of the vortex boundary is computed with a simple contour dynamics scheme (*9*), with a midpoint rule to evaluate the contour integrals and a Bulirsch-Stoer (*10*) time-stepper, with a relative accuracy per Great Dark Spot rotation period of 10^{-7} for the integrator. Because we are primarily interested in the shape of the Great Dark Spot as defined by its second order and lower moments, we do not need high spatial resolution. The computational demands of the fitting procedure have limited us to use 50 nodes to discretize the vortex boundary.

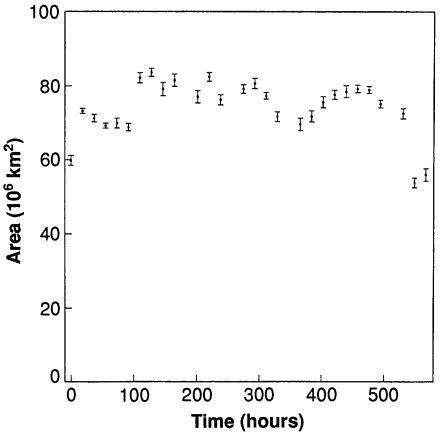

Fig. 3. The area of the Great Dark Spot versus time, as determined from our fit ellipses. The error bars in Figs. 3, 4, and 5 correspond to the uncertainties given in Table 1.

The parameters s, Π_V, and γ, together with the initial aspect ratio λ_0 and orientation φ_0 of the vortex, are determined through a standard minimization of χ^2 defined as the sum of the squares of the residuals weighted by the inverse of the estimated standard deviations. We use the Nelder-Mead downhill simplex algorithm to carry out the minimization of χ^2 (*11*). We find that the variance in the fits is larger than one would expect if the errors in Table 1 were the true errors. Because we believe the errors in Table 1 to be

Table 1. The orientation angle φ and the inverse λ of the aspect ratio, as determined by our fits to the projected Voyager images. The images are labeled by Great Dark Spot rotation periods. During some periods there were no usable images of the Dark Spot (*1*).

Frame	φ	λ
0	0.298 ± 0.013	0.431 ± 0.010
1	0.150 ± 0.006	0.478 ± 0.005
2	0.084 ± 0.001	0.501 ± 0.006
3	0.049 ± 0.011	0.512 ± 0.005
4	−0.051 ± 0.006	0.478 ± 0.002
5	−0.072 ± 0.003	0.408 ± 0.005
6	−0.001 ± 0.006	0.357 ± 0.007
7	0.006 ± 0.002	0.321 ± 0.002
8	0.052 ± 0.002	0.352 ± 0.005
9	0.059 ± 0.004	0.354 ± 0.006
10		
11	0.159 ± 0.004	0.405 ± 0.010
12	0.166 ± 0.007	0.450 ± 0.007
13	0.093 ± 0.003	0.564 ± 0.009
14		
15	−0.078 ± 0.003	0.441 ± 0.008
16	−0.079 ± 0.003	0.404 ± 0.006
17	−0.034 ± 0.003	0.344 ± 0.003
18	0.063 ± 0.003	0.357 ± 0.008
19		
20	0.131 ± 0.008	0.443 ± 0.011
21	0.154 ± 0.004	0.508 ± 0.011
22	0.135 ± 0.006	0.553 ± 0.013
23	0.077 ± 0.007	0.606 ± 0.012
24	−0.106 ± 0.006	0.590 ± 0.009
25	−0.125 ± 0.006	0.500 ± 0.003
26	−0.120 ± 0.002	0.416 ± 0.005
27	−0.035 ± 0.004	0.360 ± 0.003
28		
29	0.039 ± 0.002	0.310 ± 0.007
30	0.039 ± 0.006	0.385 ± 0.005
31	0.134 ± 0.003	0.452 ± 0.013

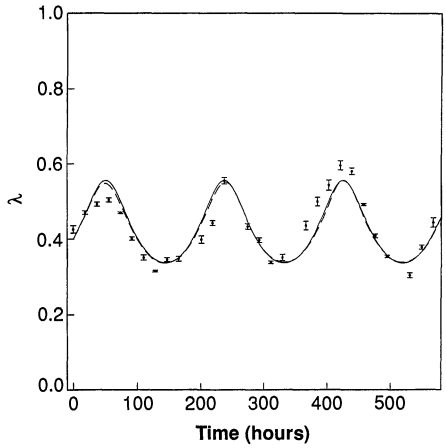

Fig. 4. The inverse of the aspect ratio versus time. The data points from our fits to the images are superimposed on the fits to the dynamical models. The solid line is the best fit of model 1. The fit for model 2 is indistinguishable from that of model 1. The dashed curve is the fit of model 3, with $\gamma = 0.00025\ km^{-1}$.

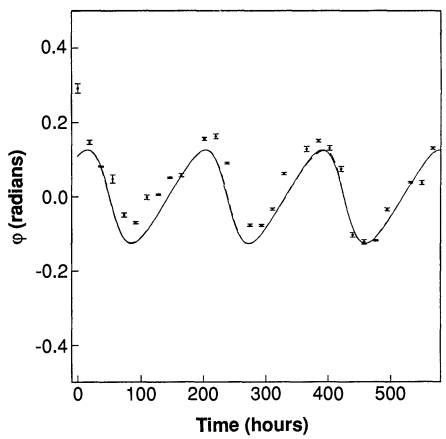

Fig. 5. The same as Fig. 4 but for the orientation angle φ.

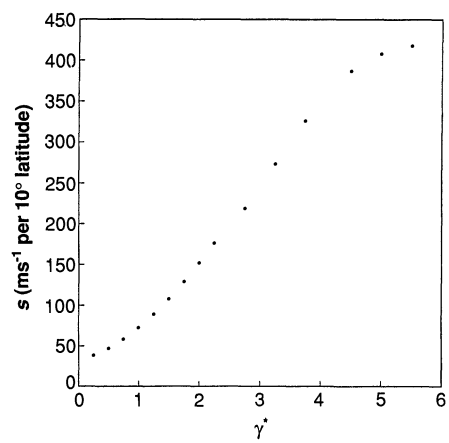

Fig. 6. Best fit values from model 3 of the background shear s around the Great Dark Spot as a function of the ratio γ^* of the diameter of the vortex to the Rossby deformation radius.

underestimates of the true errors, we have used the variance of the fit to provide a more realistic estimate of the uncertainties in the fit parameters.

Results. First, the data indicate that the elliptical shape of the Great Dark Spot is oscillating in both aspect ratio and orientation. We can describe one cycle of its oscillation as follows: beginning when the major axis is aligned with the zonal direction at maximum aspect ratio ($\varphi = 0$, minimum λ), the elliptical shape rotates counterclockwise ($\dot{\varphi} > 0$) as the aspect ratio decreases. The angle φ reaches a maximum while the aspect ratio continues to decrease. When the aspect ratio reaches its minimum the major axis is again aligned with the zonal direction ($\varphi = 0$, maximum λ). This half cycle is followed by a similar one with negative inclination ($\varphi < 0$), as the aspect ratio goes from minimum to maximum, bringing the vortex back to its initial configuration.

The animated sequence of Voyager images conveys an impression of a rolling motion (*1*). The human eye tends to follow the ends of the ellipse when it is most elongated, which occurs when $\dot{\varphi} > 0$; this gives an impression of counterclockwise rotation.

Despite its obvious inadequacies, model 1 does a remarkably good job of fitting the data. Simply choosing s/q_V in Eq. 7 so as to match the maximum and minimum aspect ratio automatically gives the amplitude of the oscillation in orientation and the shape of both curves. This model appears to capture the essential dynamics of the Great Dark Spot.

We emphasize that the data have more structure in them than is simply described by a harmonic oscillation. In particular, the plot of λ versus time has broader valleys than peaks (Fig. 4), and the plot of φ versus time has a noticeable saw-toothed appearance (Fig. 5). The simple models we have presented reproduce this structure. This is further evidence that these dynamical models are relevant to the Great Dark Spot.

An important result of our models is that the shape oscillations can only be reproduced if the vorticity of the Great Dark Spot is greater than that of the background, as is the case for the Great Red Spot.

In model 1, the detailed fits give an estimate of the vorticity in the Great Dark Spot and the background shear. We find $s = -0.954 \pm 0.045 \times 10^{-5}\ s^{-1}$ (corresponding to $46 \pm 2\ ms^{-1}$ per 10° latitude), $q_V = 1.061 \pm 0.017 \times 10^{-5}\ s^{-1}$ (with $\varphi_0 = 0.109 \pm 0.011$, $\lambda_0 = 0.4003 \pm 0.0016$). The total vorticity inside the vortex is then $q_V + q_B = q_V - s = 2.015 \pm 0.100 \times 10^{-5}\ s^{-1}$.

For these best fit parameters, we have carried out the linear stability (Floquet) analysis for the growth of two-dimensional perturbations on the vortex boundary (*15*): we find that the vortex is linearly stable (we have tested all modes with azimuthal wave number up to 100).

Our vorticity estimates improve on the earlier values of the Voyager imaging team, who estimated the total vorticity of the

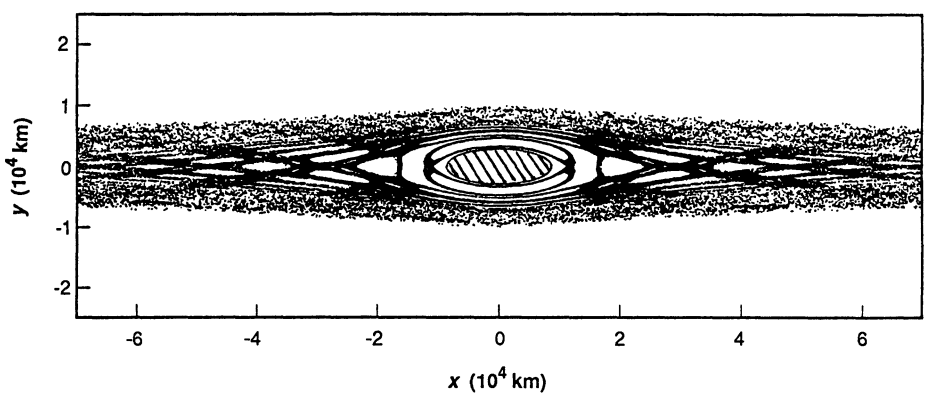

Fig. 7. A Poincaré surface of section for fluid motion near the Great Dark Spot on Neptune. The hatched region is the Great Dark Spot. The chaotic zone, represented by the scattered points, is much larger than the vortex.

Great Dark Spot to be 0.9×10^{-5} s^{-1}. That estimate was based on the apparent rolling motion, assuming that it represented fluid motion rather than a variation of shape. The Voyager imaging team (*1*) thus incorrectly concluded that the vorticity of the Great Dark Spot is smaller than the vorticity of the background, contrary to the situation for the Great Red Spot.

In model 2 the variation in the Coriolis parameter with latitude (β effect) is included. Recall, however, that since the potential vorticity is taken to be piecewise uniform in this model, the vortex cannot lose energy by Rossby wave radiation. We find that, within these limitations, the β-effect has very little influence on the evolution of the vortex shape for parameter values appropriate for the Great Dark Spot. The detailed fits are virtually identical to those of model 1.

In model 3 we choose several values of the Rossby deformation radius and, for each, fit for the same parameters as in the previous models. For values of the Rossby deformation radius that are larger than the size of the vortex, the dynamics is found to be qualitatively similar to that of the first two models. When the vortex becomes larger than the Rossby deformation radius, however, the distortion of the elliptical shape becomes severe. Figure 6 shows the fit values of the background shear s versus the ratio γ^* of the diameter D of the vortex to the Rossby deformation radius.

The Voyager imaging team reported (*1*) a value of the background shear at the latitude of the Great Dark Spot of 100 ms^{-1} per 10° latitude, determined from a simple linear fit to the zonal velocity profile as obtained from the motion of large features at the latitude of the Great Dark Spot and further south. The features further north suggest that the zonal velocity profile is better represented by a parabolic shape, and thus the true shear near the Great Dark Spot is likely to be smaller than the value reported by the Voyager imaging team. Taking the value of 100 ms^{-1} per 10° latitude as an upper bound, we infer from Fig. 6 that γ^* has to be less than 1.4, and hence that the Rossby deformation radius is probably greater than approximately 7000 km (or about two thirds the diameter of the Great Dark Spot).

It has been shown (*16*) that vortex dynamics in the equivalent barotropic system (model 3) is characterized by a strong suppression of vorticity filamentation at large values of γ^*. Typically, filaments are observed during vortex merger only for $\gamma^* < 3$. The fact that our fits suggest a value of γ^* between 1 and 2 in the vicinity of the Great Dark Spot is consistent with the observation of filaments being expelled around the vortex (*1*) (see, for instance, Fig. 2).

Planetary scale chaos. The motion of individual fluid elements, given by Eq. 3, can be described in Hamiltonian terms, where the streamfunction ψ is the Hamiltonian, and the Cartesian coordinates y and x of a fluid element play the role of the canonical coordinate and conjugate momentum, respectively. The oscillations in shape of the vortex imply a time-dependent streamfunction, and thus the motion of fluid element is governed by a one degree-of-freedom time-dependent Hamiltonian. This system is complicated enough for some trajectories to exhibit chaotic motion (*17*). In fact, we have shown (*8*) that there are often large regions of chaotic advection surrounding the sheared elliptical vortices of model 1, depending on the parameters chosen. It turns out that this is the case for the parameters determined from the fit to the oscillations of the Great Dark Spot.

The chaotic zones of a dynamical system are most easily exhibited by computing Poincaré surfaces of section. For model 1 the shape oscillations are periodic, and a convenient Poincaré section is generated by looking at the fluid motion stroboscopically, that is by plotting the successive positions of fluid elements after every vortex oscillation period. A Poincaré section for model 1, with the best fit parameters for the Great Dark Spot, is shown in Fig. 7 (two initial conditions only were used to obtain this figure). The scattered dots indicate a chaotic zone which is enormous given the size of the Great Dark Spot (recall that the diameter of the Great Dark Spot is comparable to the size of the Earth).

The characteristic property of chaotic motion is that nearby trajectories diverge exponentially from one another. The mean exponential rate of divergence is measured by the Lyapunov exponent, which we have computed for the fluid motion near the Great Dark Spot. We find that the time scale for exponential divergence of nearby trajectories is approximately ten vortex oscillation periods, which corresponds to about 80 days since the period of the vortex oscillation is about 8 days.

The calculation of the extent of the chaotic zones for model 2 and model 3 are too computationally demanding for us to carry out. However, we expect that the qualitative nature of the fluid trajectories will not change. Several important features of the fluid trajectories will be preserved. For instance, for a stationary vortex there must always be an infinite period trajectory which separates the fluid which is trapped by the vortex from the fluid which is carried away by the shear flow. The presence of a separtrix is a crucial ingredient for the presence of chaotic behavior. When time dependence, such as that associated with the vortex oscillations, is present, separatrices generically broaden into chaotic zones. For models with more general distributions of potential vorticity, we expect that the streamlines will have similar qualitative features and thus it is plausible to expect that chaotic zones will exist for similar reasons. In fact, the presence of these planetary-scale chaotic zones may provide a dynamical mechanism for the homogenization of the potential vorticity in the vicinity of oscillating vortices.

Addendum on Jovian vortices. The Kida equations (Eq. 7) also provide a rather good zeroth-order model for the dynamics of Jovian vortices. For the Great Red Spot, there is evidence that the potential vorticity is in fact not uniform (both in and around the vortex) and that the topography of the lower layer plays an important role in the potential vorticity balance (*12*); moreover, the flow surrounding this vortex is a linear shear over only approximately two thirds of the latitudinal extent of the Great Red Spot (*14*), and the size of that vortex is believed to be large compared to the local Rossby deformation radius. These considerations notwithstanding, we show that the Kida equations are able, in spite of their simplicity, to capture the order of magnitude dynamics for both the Great Red Spot and the White Oval BC of Jupiter.

For these vortices the aspect ratio λ and inclination φ appear to be essentially time-dependent. Requiring the solutions of Eq. 7 to be stationary yields a unique relation between the aspect ratio λ of the vortex and the ratio q_B/q_V of the background to anomalous vorticities:

$$\frac{q_B}{q_V} = \frac{1 - \lambda}{\lambda(1 + \lambda)} \tag{14}$$

provided the major axis is aligned with the zonal direction ($\varphi = 0$).

The aspect ratio of the Great Red Spot is approximately 2.0 ± 0.2 (*12*), the average value of the anomalous vorticity is roughly $q_V = 1.7 \pm 1.0 \times 10^{-5}$ s^{-1} (*13*) and, from the zonal velocity profile given by Limaye (*14*), we estimate the background vorticity to be $q_B = 1.3 \pm 0.2 \times 10^{-5}$ s^{-1}. This yields a ratio $q_B/q_V = 0.76 \pm 0.46$, in satisfactory agreement the value $q_B/q_V = 0.66 \pm 0.10$ from Eq. 14. For the White Oval BC the aspect ratio is 1.66 ± 0.10 (*12*), $q_B = 1.3 \pm 0.2 \times 10^{-5}$ s^{-1}, and $q_V = 3.7 \pm 2.0 \times 10^{-5}$ s^{-1}, so that $q_B/q_V = 0.35 \pm 0.19$. Again, this agrees well with the value 0.41 ± 0.06 from Eq. 14 required for a stationary vortex of this aspect ratio.

Considering the simplicity of our models and the uncertainty in our knowledge of the vorticities, the agreement in both cases is good. The fact that the predictions of model 1 are in reasonable

agreement with the data for the Great Red Spot and the White Oval BC on Jupiter lends support to our application of these simple models to the Great Dark Spot of Neptune for which there is less direct velocity data.

Finally, we point out that it would be of great interest to use the models we have presented here to perform fits to the "brown barge" type vortices on Jupiter (*18*), whose aspect ratios have been observed to vary by as much as 10% over a 15-day period, and for which the vorticity can be directly measured from velocity vectors.

REFERENCES AND NOTES

1. B. A. Smith *et al.*, *Science* **246**, 1422 (1989).
2. Recall that geostrophy is characterized by the balance between the pressure gradient and the Coriolis force. Quasigeostrophy describes the time evolution of a flow in geostrophic balance.
3. P. S. Marcus, *Nature* **331**, 693 (1988).
4. J. Sommeria *et al.*, *ibid.*, p. 689.
5. J. Pedlosky, *Geophysical Fluid Dynamics*, (Springer-Verlag, New York, 1979).
6. The modeling of a presumably internally heated, compressible, continuously stratified and baroclinic atmosphere with essentially two-dimensional incompressible and adiabatic models is supported in part by the normal mode analysis of R. K. Achterberg and A. P. Ingersoll [*J. Atmos. Sci.* **46**, 2448 (1989)].
7. S. Kida, *J. Phys. Soc. Japan* **50**, 3517 (1981).
8. L. M. Polvani and J. Wisdom, in *Topological Aspects of Fluid Motion*, H. K. Moffat Ed. (Cambridge University Press, Cambridge, 1990), and also L. M. Polvani and J. Wisdom, *Phys. Fluids A* **2**, 123 (1990).
9. N. J. Zabusky, M. H. Hughes, K. V. Roberts, *J. Comp. Phys.* **30**, 96 (1979).
10. R. Bulirsch and J. Stoer, *Numerische Math.* **8**, 1 (1966).
11. J. A. Nelder and R. Mead, *Comp. J.* **7**, 308 (1965).
12. T. E. Dowling and A. P. Ingersoll, *J. Atmos. Sci.* **45**, 1380 (1988).
13. As we have pointed out, the vorticity inside the Great Red Spot is not uniform [see (*12*) and J. L. Mitchel, R. F. Beebe, A. P. Ingersoll, G. W. Garneau, *J. Geophys. Rev.* **86**, 8751 (1981)]. The vorticity is small near the center and is maximum in an annular ring with peak values near 5×10^{-5} s^{-1}. We estimate the area weighted mean vorticity to be roughly $3 \pm 1 \times 10^{-5}$ s^{-1}.
14. S. S. Limaye, *Icarus* **65**, 335 (1986).
15. For a complete description of the linear and nonlinear stability analysis of the Kida solutions see D. G. Dritschel, *J. Fluid Mech.* **206**, 193 (1990) and also S. P. Meacham, G. R. Flierl, U. Send, *Dynam. Atmos. Oceans* **14**, 333 (1990).
16. L. M. Polvani, N. J. Zabusky, G. R. Flierl, *J. Fluid Mech.* **205**, 215 (1989). See also D. G. Dritschel, *Comp. Phys. Rep.* **10**, 77 (1990).
17. For background on chaotic behavior in Hamiltonian systems see, for example, the articles in *Hamiltonian Dynamical Systems*, R. S. MacKay and J. D. Meiss, Eds. (Adam Hilger, Bristol, 1987).
18. A. Hatzes, D. D. Wenkert, A. P. Ingersoll, G. E. Danielson, *J. Geophys. Res.* **86**, 8745 (1981).

19. We thank G. Flierl and P. Marcus for interesting conversations. The shape oscillations of the Great Dark Spot were originally observed by H. Hammel and L. Sromovski. J.W. gratefully acknowledges support from the NASA Planetary Geology and Geophysics Program (NAGW-706) and the NSF Presidential Young Investigator Program (AST-8857365). L.M.P. gratefully acknowledges support from the Atmospheric Science Division of the NSF under grant 8911459-ATM. E.D. and A.P.I. acknowledge the support of the Voyager Project, and the NASA Planetary Atmospheres Program (NAGW-58).

Structure of Ribonuclease H Phased at 2 Å Resolution by MAD Analysis of the Selenomethionyl Protein

WEI YANG, WAYNE A. HENDRICKSON, ROBERT J. CROUCH, YOSHINORI SATOW

Ribonuclease H digests the RNA strand of duplex RNA·DNA hybrids into oligonucleotides. This activity is indispensable for retroviral infection and is involved in bacterial replication. The ribonuclease H from *Escherichia coli* is homologous with the retroviral proteins. The crystal structure of the *E. coli* enzyme reveals a distinctive α-β tertiary fold. Analysis of the molecular model implicates a carboxyl triad in the catalytic mechanism and suggests a likely mode for the binding of RNA·DNA substrates. The structure was determined by the method of multiwavelength anomalous diffraction (MAD) with the use of synchrotron data from a crystal of the recombinant selenomethionyl protein.

RIBONUCLEASES H (RNASE'S H) CONSTITUTE A FAMILY OF enzymes that hydrolyze RNA molecules only when hybridized with complementary DNA strands (*1*). Although this activity is distributed broadly, the biological role of RNase H is poorly characterized, except in the instances of *Escherichia coli* and retroviruses. RNase H participates in DNA replication in *E. coli*; it helps to specify the origin of genomic replication by suppressing initiation at origins other than the locus oriC (*2, 3*); along with the 5′ → 3′ exonuclease of DNA polymerase I, it removes RNA primers from the Okazaki fragments of lagging strand synthesis (*4*); and it defines the origin of replication for ColE1-type plasmids by specific cleavage of an RNA preprimer (*5*). However, these do not appear to be vitally important activities since *rnh*$^-$ mutants of *E. coli* survive except in conjunction with certain other genetic defects (*3, 6, 7*). By contrast, RNase H activity is absolutely indispensable for retroviral replication. The RNase H of retroviruses is a component of reverse transcriptase (RT) (*8, 9*). Briefly stated, during reverse transcription the polymerase moiety of the transcriptase uses the genomic RNA as a template for synthesis of an RNA·DNA intermediate; RNase H then removes the RNA to free the complementary DNA strand which serves as the template for plus strand synthesis; and finally the resulting DNA duplex can be integrated into the host genome.

W. Yang and W. A. Hendrickson are in the Department of Biochemistry and Molecular Biophysics, Columbia University, New York, NY 10032 where W.A.H. is also an investigator with the Howard Hughes Medical Institute. R. J. Crouch is at the Laboratory of Molecular Genetics, National Institute of Child Health and Human Development, National Institutes of Health, Bethesda, MD 20892. Y. Satow is at the Faculty of Pharmaceutical Sciences, University of Tokyo, Hongo, Bunkyo-ku, Tokyo 113, Japan, and also at the Photon Factory, National Laboratory for High Energy Physics, 1-1 Oho, Tsukuba-shi, Ibaraki 305, Japan.